Journal of Oceanology and Limnology

https://doi.org/10.1007/s00343-026-5506-9

Research Paper

Optical retrieval of sea surface wave parameters using China's HY-1E Coastal Zone Imager*

Lifeng WANG[1], Qingjun SONG[2], Mingxiu WANG[1], Sheng YANG[2], Ziyao YIN[1], Jun TANG[1], Hang LÜ[1], Keli ZHANG[3], Yuze CAO[3], Lili WANG[3], Yuntao WANG[4], Yingcheng LU[1, **]

[1] *International Institute for Earth System Science, Collaborative Innovation Center of South China Sea Studies, Nanjing University, Nanjing 210023, China*

[2] *National Satellite Ocean Application Service, Ministry of Natural Resources, Beijing 100081, China*

[3] *DFH Satellite Co., Ltd., Beijing 100094, China*

[4] *Second Institute of Oceanography, Ministry of Natural Resources, Hangzhou 310012, China*

Received Dec. 15, 2025; accepted in principle Feb. 11, 2026; accepted for publication Apr. 9, 2026

Abstract High resolution satellite optical sensors provide detailed sea surface textures and wave patterns, offering significant potential for retrieving sea surface wave parameters. The Coastal Zone Imager (CZI) onboard China's ocean color satellite Haiyang-1E (HY-1E) provides 20-m multispectral and 5-m panchromatic imagery with a 3-d revisit cycle. Its distinctive optical design, which separates transmission and reflection channels onto different focal planes, introduces specific along-track channel time lags. In this study, the viewing geometry and inter-channel time lags of the CZI sensor were systematically evaluated. A dedicated workflow for wave parameter retrieval was developed and its feasibility was validated using 4 in-situ measurements and 69 reanalysis matchups. There is a statistically linear relationship between CZI-derived and reanalysis wave direction (RMSE=20.50°, Bias=0.24°) and period (RMSE=1.68 s, Bias=0.10 s). The specific requirements and limitations of CZI for resolving the 180° directional ambiguity were analyzed in detail. Furthermore, the proposed method was applied to generate the original coastal regional wave products from HY-1E. The uncertainty in comparison with ERA5 products and the potential of wind speed estimation were additionally discussed. Overall, these findings demonstrate that the HY-1E CZI sensor can effectively retrieve sea surface wave parameters, providing a valuable data source for monitoring coastal and marine dynamical environments.

Keyword: sea surface wave; optical remote sensing; Haiyang-1E (HY-1E) Coastal Zone Imager (CZI); wave parameter; time lag

1 INTRODUCTION

Sea surface waves are the most fundamental and critical dynamic elements in oceanography, which modulate the upper-ocean circulation and act as a vital component for exchanges of momentum, heat, and water vapor across the air-sea interface (Yin et al., 2024; Ma et al., 2026). These processes directly influence the stability of the marine atmospheric boundary layer (MABL) and turbulent transport (Wang et al., 2019; Stopa et al., 2022). Accurate acquisition of wave parameters is essential for coastal engineering, navigation safety, offshore ecological management, and marine disaster prediction.

At present, the observations of surface waves rely on in-situ measurements and remote sensing. In-situ wave observations, such as moored buoys, survey vessels and stationary platforms, provide

* Supported by the National Key Research and Development Program of China (No. 2023YFB3905802), the National Natural Science Foundation of China (No. 42371380), the Civil Space Technology Advance Research Project of China (No. D010202), and the Fundamental Research Funds for the Central Universities (No. 0904-14380035)

** Corresponding author: luyc@nju.edu.cn

high-accuracy, multi-parameter records, but limitation of sparse spatial coverage and high maintenance costs. Thus, it is not suitable for large-scale and continuous ocean monitoring. Satellite remote sensing provides a low cost and wide coverage survey technique for global oceans. For instance, synthetic aperture radar (SAR) provides an all-day and all-weather capability for global wave observation (Zhang et al., 2015; Mouche et al., 2019; Wang et al., 2019). The wave spectra can be derived through a nonlinear integral model (Hasselmann and Hasselmann, 1991). Recently, data-driven/artificial intelligence (AI) approaches have also demonstrated promising performance for sea-state and wave-related parameter estimation (Hao et al., 2025). Nevertheless, SAR wave retrieval still faces certain limitations such as the Doppler shift effect and the quality of suitable datasets. The Surface waves investigation and monitoring (SWIM) instrument onboard the China-France Oceanography Satellite (CFOSAT) can provide directional wave spectra and significant wave height on a global scale (Hauser et al., 2017; Wang et al., 2025c). However, its spatial resolution is relatively coarse and unsuitable for coastal ocean observations.

Optical remote sensing provides widely available data with high spatial resolution over both coastal and open ocean regions. Due to the brightness modulation by sunglint and sky radiance, wave textures can be clearly observed in high resolution optical images (Cox and Munk, 1954; Hu et al., 2009; Jackson and Alpers, 2010). Previous methods based on the linear dispersion relation, Fast Fourier Transform (FFT), and transfer functions enable the retrieval of nearshore bathymetry, wave motion, and wave spectra from such imagery (De Michele et al., 2012; Kudryavtsev et al., 2017a; Yurovskaya et al., 2018, 2019; Bergsma et al., 2019). Furthermore, the inherent time lag in push-broom sensors can be used to resolve the 180° directional ambiguity in wave propagation (Kudryavtsev et al., 2017a, b; Wang et al., 2025a, b). The feasibility of these techniques has been validated with several optical spaceborne sensors such as Sentinel-2 Multispectral instrument (MSI), Landsat-8 Operational Land Imager (OLI), and SPOT-5. However, how to extend the optical methods to other satellite sensors, and the impacts of different spatial resolution and optical configuration remain insufficiently investigated.

China's new-generation ocean color satellite Haiyang-1E (HY-1E), launched in November 2023, carried multiple advanced payloads including the Color and Temperature Scanner (COCTS, Bai et al., 2025), the Medium-resolution Programmable Imaging Spectrometer (MPIS), and the Second-generation Coastal Zone Imager (CZI or CZI2, hereafter called CZI). The CZI is equipped with eight multispectral channels and a panchromatic channel (Zhang et al., 2025a, b). In side-swing mode, it achieves 60-km swath with 3-d effective revisit over 1 000-km cross-track coverage, and its multispectral resolution is better than 20 m (Zheng et al., 2025). Such detailed spatial observations capture fine sea surface features as shown in Fig.1, including floating targets (algae, slicks) and dynamical patterns (whitecaps, cells, wind streaks, fronts, internal waves), thereby providing new means for ocean dynamic monitoring. However, several key issues remain to be addressed using CZI data: (1) how to develop a wave retrieval strategy adapted to the CZI sensor? (2) what impacts the unique optical design of CZI on wave retrieval? (3) what are the limitations and uncertainties of CZI-derived products?

In this paper, we aim to resolve the above issues to evaluate the wave monitoring capabilities of the CZI onboard HY-1E. The structure is as follows: The satellite and validation dataset, and the methodologies are introduced in Section 2. The method implementation and validation are given in Section 3, including the analysis of the impact on dual-focal-plane design for wave parameter estimation and the development of regional wave product. The uncertainty of the method and the additional advantages by CZI are discussed in Section 4. Overall, this work provides both theoretical insight and technical support for the application of China's ocean color satellite in quantitative monitoring of marine dynamic environments.

2 DATA AND METHOD

2.1 HY-1E CZI data

China's new-generation ocean color satellite HY-1E was launched in November 2023 and completed its in-orbit testing in October 2024, after which operational CZI products became available on National Satellite Ocean Application Service (NSOAS, https://osdds.nsoas.org.cn/DataRetrieval). The sensor operates at an orbital altitude of 782 km, providing a 60-km swath width for a single scene. In the side-swing mode, the observation range can be extended to over 1 000 km and a global revisit cycle

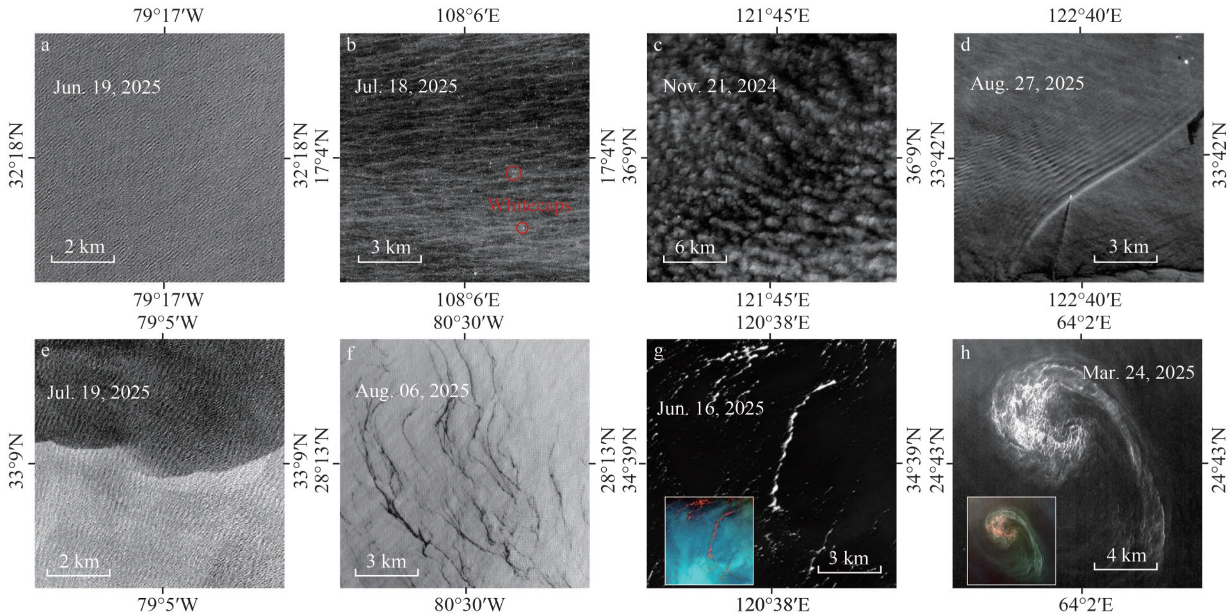

Fig.1 Sea surface features in B7 images (830 nm) of HY-1E CZI

a. pure waves; b. wind-generated streaks and whitecaps; c. micro convective cells; d. internal waves; e. oceanic fronts; f. slicks; g. floating algae; h. eddies with algal bloom; the inserts in (g) and (h) are false-color composite images (R: 830 nm, G: 660 nm, B: 555 nm).

of 3 d. As shown in Table 1, it consists of 8 multispectral channels spanning the visible to near-infrared band, with a nadir spatial resolution of 20 m, and a panchromatic channel with 5-m resolution. The signal-to-noise ratio exceeds 200 for all channels.

The optical configuration of CZI is illustrated in Fig.2a, incident light is first reflected by the swing lens and then enters the primary optical system for focusing. A wedge-shaped spectroscope divides the focused light into two optical paths: a reflection path (5 channels focal plane) and a transmission path (4 channels focal plane). The optical signals are subsequently captured by TDICCD detectors and converted into electrical signals, producing digital imagery for the nine spectral bands (Zhang et al.,

Table 1 Band configuration of CZI

Band ID	Central wavelength (nm)	Bandwidth (nm)	S/N
1	425	50	≥300
2	485	70	≥300
3	555	70	≥300
4	605	40	≥300
5	660	60	≥300
6	725	40	≥200
7	830	120	≥200
8	950	180	≥200
P	625	350	≥200

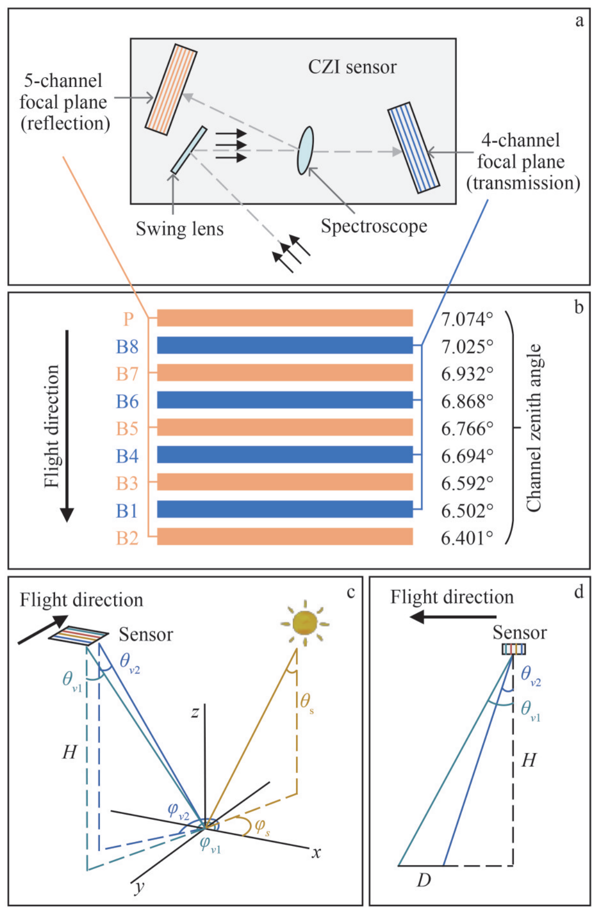

Fig.2 CZI sensor configuration and imaging principle

a. CZI sensor specific optical configuration; b. channel arrangement and imaging zenith angle; c. sketch of CZI imaging geometry; d. side view of imaging geometry (ignoring azimuth angle).

2025a, b; Zheng et al., 2025). Due to this specific optical configuration of CZI, viewing angle differences exist between adjacent channels and across the two separate reflection and transmission focal planes. Figure 2b illustrates the sensor zenith angles corresponding to the 9 channels, where the orange boxes denote the reflection channels and the blue boxes denote the transmission channels. Among these channels, B2 is acquired first along the flight direction, whereas the panchromatic band is imaged last. These subtle differences in viewing geometry (Fig.2c) lead to inter- and cross-focal plane time lags, which can be calculated as follows:

$$\Delta t = D/V, \tag{1}$$

$$D = H\sqrt{\tan^2\theta_{v1} + \tan^2\theta_{v2} - 2\tan\theta_{v1}\tan\theta_{v2}\cos\left(\varphi_{v1} - \varphi_{v2}\right)}, \tag{2}$$

where H denotes the sensor orbital altitude (782 km), V represents the satellite velocity (7.44 km/s), D is the length of satellite track, θ_{v1}, θ_{v2} and φ_{v1}, φ_{v2} are the zenith and azimuth view angles in two different bands. Since the official HY-1E documentation does not provide the azimuth angle of spectral channels, and considering that the variation in relative azimuth for the same ground target is minimal (i.e., $\cos(\varphi_{v1} - \varphi_{v2}) \approx 1$), the viewing geometry can be simplified as depicted in Fig.2d. Thus, Eq.1 reduces to:

$$\Delta t = H\left|\tan\theta_{v1} - \tan\theta_{v2}\right|/V. \tag{3}$$

The resulting time lags and their specific applications are detailed in Section 3. The CZI data used in this study are the Level-2A Rayleigh-corrected reflectance (R_{rc}) products from the NSOAS, and have a cloud cover of less than 5%. The raw products are HDF5 format and were geometrically corrected using the Georeferenced Lookup Table (GLT) tool in ENVI 5.6.

2.2 In-situ buoy and reanalysis data

2.2.1 NDBC buoy

The hourly standard meteorological data and wave spectra from the National Data Buoy Center (NDBC) were utilized to validate CZI-derived wave parameters. Four HY-1E CZI-buoy matchup pairs covering the U.S. East and West Coast were collected, including buoy station ID 41004 (32.50°N, 79.08°W) and 46086 (32.50°N, 118.03°W) as shown in Fig.3a & b. The time difference between satellite imaging and in-situ measurements was <20 min, and the spatial distance was <10 km for the matched cases. The used NDBC wave parameters include the mean wave direction (MWD), defined as the direction from which waves at the dominant period are coming, relative to true north and increasing clockwise, and the dominant wave period (DPD). The wave spectra provided by NDBC are derived from five Fourier coefficients, and in this study, the maximum entropy method (MEM) was applied to reconstruct the wave spectra (Lygre and Krogstad, 1986; Fan et al., 2023). The spectra are normalized to a range of 0–1, and the dominant wavelength (WL) of the MWD is subsequently calculated.

2.2.2 ECMWF ERA5

The European Centre for Medium-Range Weather Forecasts (ECMWF) fifth-generation reanalysis (ERA5) provides hourly estimations of atmospheric, oceanic, and land-surface variables over the past eight decades. In this study, a total of 69 sets of hourly ERA5 wave products matched with CZI observations were used to verify the accuracy of the retrieved wave parameters. Each matched CZI segment was set as 400×400 pixels (8 km×8 km), and their spatial distribution is shown in Fig.3c. The selected matchups have wind speeds ranging from 3 to 12 m/s to avoid interference of extreme environments. The 0.5° resolution ERA5 products of MWD and mean wave period (MWP) were employed. In addition, ERA5 data were used to validate the regional CZI-derived wave products. These products have a resolution of 4×4 km and were binned to a 0.5°×0.5° grid for comparison with the ERA5 MWD product.

2.3 Method for wave parameters retrieval

Considering the specific optical configuration and imaging characteristics of the CZI sensor, the overall workflow for retrieving ocean wave parameters from CZI imagery can be divided into three major steps, as illustrated in Fig.4. First, the Level-2A R_{rc} product is subjected to geometric correction, and high-pass filtering is applied to reduce the interference of thin clouds and background targets. Two spectral bands (e.g., B2 and B7) are selected, and the time lag between them is calculated using Eq.3. Secondly, FFT is applied independently to the two selected bands. The FFT window size is 400×400 pixels, which has been proven to be the optimal window for regional wave retrieval (Wang et al., 2025b). Cross-spectral

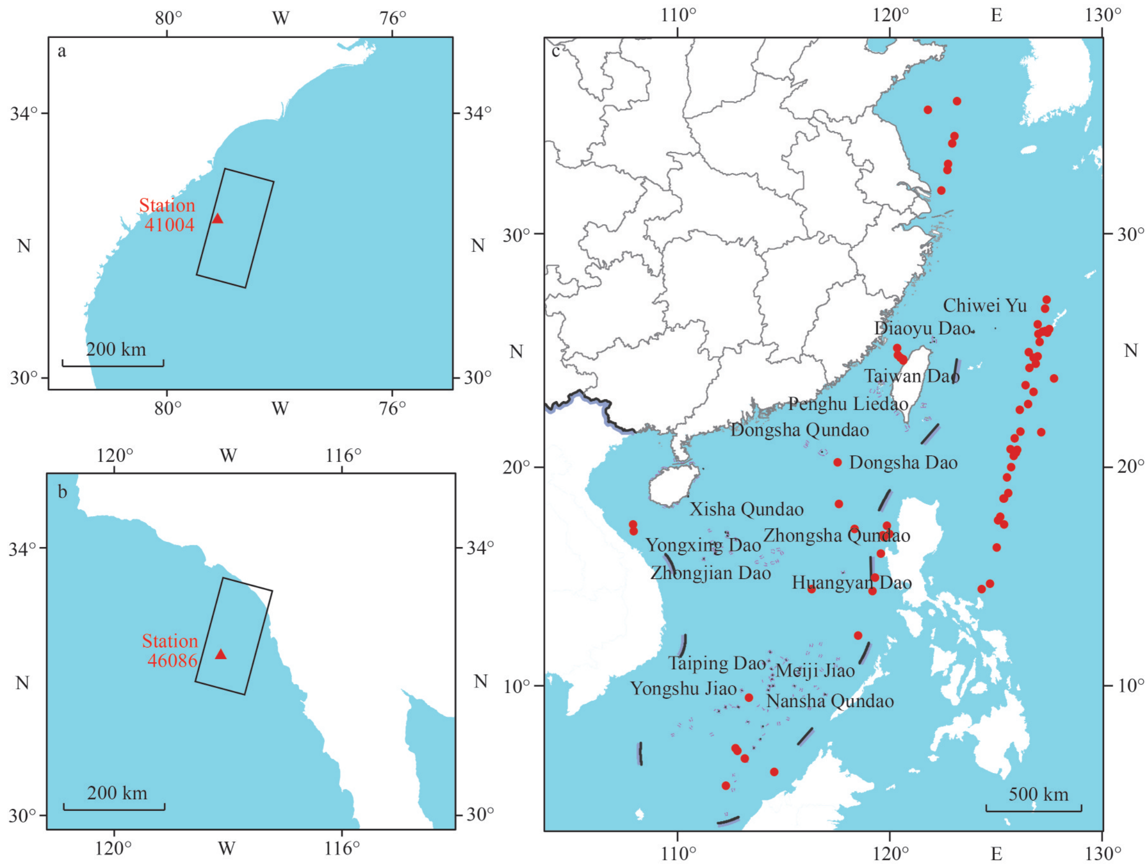

Fig.3 Location of the in-situ and reanalysis data matchups to HY-1E CZI observations

a. NDBC station on U.S. East coast; b. NDBC station on U.S. West coast; c. ERA5 matchups over the Western Pacific Ocean. Map review No. GS(2020) 4619.

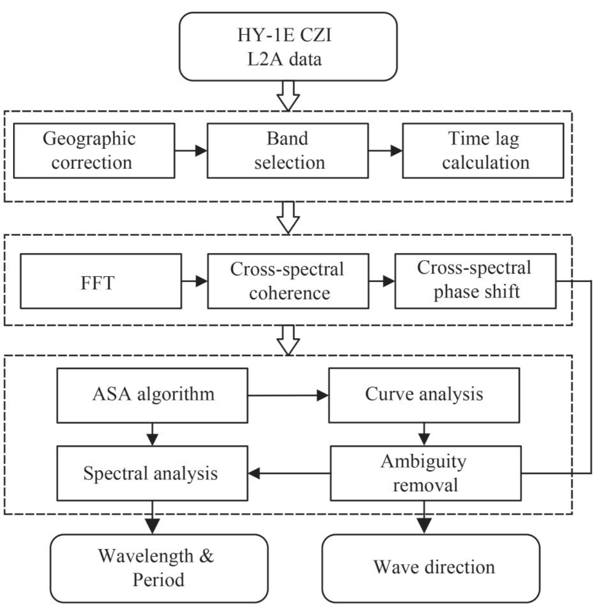

Fig.4 Overall flowchart of wave parameters retrieval

analysis is subsequently performed to quantify the coherence $C(I_1, I_2)$ and phase shift $P(I_1, I_2)$ of cross spectrum between the two bands (Kudryavtsev et al., 2017a):

$$C\left(I_1,I_2\right)=\left(\widehat{I_1}\widehat{I_2}^*\right)^2/\left(\widehat{I_1}\widehat{I_1}^*\cdot\widehat{I_2}\widehat{I_2}^*\right), \tag{4}$$

$$P\left(I_1,I_2\right)=\arg\left(<\widehat{I_1}\widehat{I_2}^*>\right), \tag{5}$$

$$\left(k_x,k_y\right)=\left(\frac{2\pi i_x}{N_xD_x},\frac{2\pi i_y}{N_yD_y}\right),\quad i_x=-\frac{N_x}{2},\cdots,\frac{N_x}{2},\quad i_y=-\frac{N_y}{2},\cdots,\frac{N_y}{2}, \tag{6}$$

where I_1 and I_2 are the selected band images, the hat means the FFT, and the asterisk represents the complex conjugation. k_x and k_y denote the coordinates in the Nyquist wavenumber domain, $N_x\times N_y$ represent the pixel dimensions of the original CZI image, and $D_x\times D_y$ are the spatial resolutions of the CZI multispectral imagery (20 m).

Finally, wave parameters are computed based on spectral characteristics, divided into two sub-steps:

(1) The Angular Spectrum Analysis (ASA) method (Wang et al., 2025a) is applied to transform the two-dimensional frequency domain spectrum into a one-dimensional curve. Curve fitting and peak detection were applied to the ASA curve to obtain a directional pair with a 180° modulus. The true wave propagation direction is determined as the sign from positive to negative of the cross-spectral phase shift (Kudryavtsev et al., 2017a); (2) the energy peak M of FFT spectrum is identified along the CZI-derived direction. In the selection of multiple wave systems, the pair of spectral peaks with the highest energy was selected for analysis. The corresponding WL λ_m and wave period T_m are then calculated as (Yurovskaya et al., 2019):

$$\lambda_m = 2\pi / \sqrt{k_{x_m}^2 + k_{y_m}^2}, \quad (7)$$

$$c_m = \frac{P_m}{k_m \Delta t}, \quad (8)$$

$$T_m = \lambda_m / c_m, \quad (9)$$

where P_m is the phase shift (in radians) at the M point in the cross-spectral phase shift, c_m is the wave phase speed, k_m is the corresponding wavenumber, and Δt is the time lag of selected bands. Through the above workflow, dominant wave direction (WD), WL, and wave period can be systematically extracted from the CZI Level-2A imagery.

3 RESULT

3.1 Inter-channel time lag of HY-1E CZI

The multichannel push-broom design of optical spaceborne sensors introduces inherent time lags among different spectral bands. Systems such as Sentinel-2 MSI and Landsat-8 OLI utilize this characteristic to detect ground or sea surface phenomena including clouds, aircraft, plumes, and even oceanic dynamical processes (De Michele et al., 2016; Yurovskaya et al., 2019; Liu et al., 2020). Given that the time lags are generally much smaller than the pixel acquisition interval of physical targets (e.g., currents, wave propagation, cloud movement), accurate estimation of inter-channel delays is essential for minimizing linear errors. This section provides a detailed calculation of the inter-channel time lags of the HY-1E CZI sensor.

Unlike imaging configurations such as MSI and OLI, whose optical elements place all detectors on a single focal plane (with MSI employs twelve staggered detector clusters, European Space Agency, 2015), the CZI sensor adopts a hybrid optical focal plane system with multiple reflections and transmissions. Incident light is split by a spectroscope and directed into four transmission channels (B1, B4, B6, B8) and five reflection channels (B2, B3, B5, B7, P). Such two sets of channels are arranged on different focal planes, and the optical signals are subsequently merged by electronic conversion into a whole scene CZI imagery. As a result, a viewing geometry discrepancy arises between the transmission and reflection channels. Although the HY-1E technical documentation provides zenith angles for each channel, it does not specify the corresponding azimuth angle variations, which are required to accurately quantify the angular differences between the two focal planes. Therefore, when Eq.3 is used to estimate the inter-band time lags, it is necessary to distinguish the inter- and cross-focal plane. The former is unaffected by azimuth deviations, while the latter may contain additional imaging pixel offsets.

Figure 5 presents the inter-channel time lags of CZI derived from Eq.3, referenced to the earliest acquisition band B2. The maximum imaging time lag is 1.26 s for the B2 and panchromatic bands. Blue and orange squares indicate the two different focal planes. Light gray squares denote the two bands on the same focal plane, with no additional pixel offsets here. For the dark gray squares, there is no additional error in the time lag, but the images between different channels exist certain pixel offsets. The impact of this misregistration on wave estimation is analyzed in detail in Section 3.3.

3.2 Validation of CZI-retrieved wave parameter

In this section, the effectiveness of the CZI-based wave retrieval method is evaluated using four matched CZI-buoy and 69 ERA5 matchups. Given

Δt (s)	B2	B1	B3	B4	B5	B6	B7	B8	P
B2	/	0.19	0.36	0.55	0.68	0.87	0.98	1.17	1.26
B1	-0.19	/	0.16	0.35	0.49	0.68	0.79	0.98	1.07
B3	-0.36	-0.16	/	0.18	0.32	0.51	0.62	0.81	0.90
B4	-0.55	-0.35	-0.18	/	0.13	0.33	0.43	0.62	0.71
B5	-0.68	-0.49	-0.32	-0.13	/	0.18	0.29	0.48	0.58
B6	-0.87	-0.68	-0.51	-0.33	-0.18	/	0.11	0.30	0.39
B7	-0.98	-0.79	-0.62	-0.43	-0.29	-0.11	/	0.19	0.28
B8	-1.17	-0.98	-0.81	-0.62	-0.48	-0.30	-0.19	/	0.09
P	-1.26	-1.07	-0.90	-0.71	-0.58	-0.39	-0.28	-0.09	/

Inter-focal plane   Cross-focal plane

Fig.5 The inter-channel time lag (relative to the earliest acquisition) in CZI

the stable absorption characteristics of water in the near-infrared band (830 nm) across varying transparency conditions, and the fact that bands B2 to B7 are located on the same focal plane with a suitable inter-band time lag of 0.98 s, B2 and B7 were selected as the feature bands for subsequent processing.

Figure 6 shows the wave retrieval and validation for the four match-up cases. All four CZI scenes exhibit distinct wave patterns. Specifically, case 1 contains wave systems from multiple directions, case 2 is the wave system with a uniform propagation direction, case 3 shows wind-generated streaks, and case 4 displays clear swells. WD were derived from the FFT spectra using the ASA algorithm, where the red dashed lines in the FFT spectra indicate WD pairs and M denotes the maximum energy in such direction. The WL was calculated using the method described in Section 2.3. The 180° directional ambiguity was resolved through the sign of the phase shift P (B2, B7), where the orientation from positive to negative phase shift identifies the true propagation direction. The retrieved WLs and WDs were further compared with the in-situ buoy wave spectra (the white dashed line and circle represent the buoy-measured MWD and WL). Across 4 cases, whether dominated by locally wind-generated waves of case 1 or long-

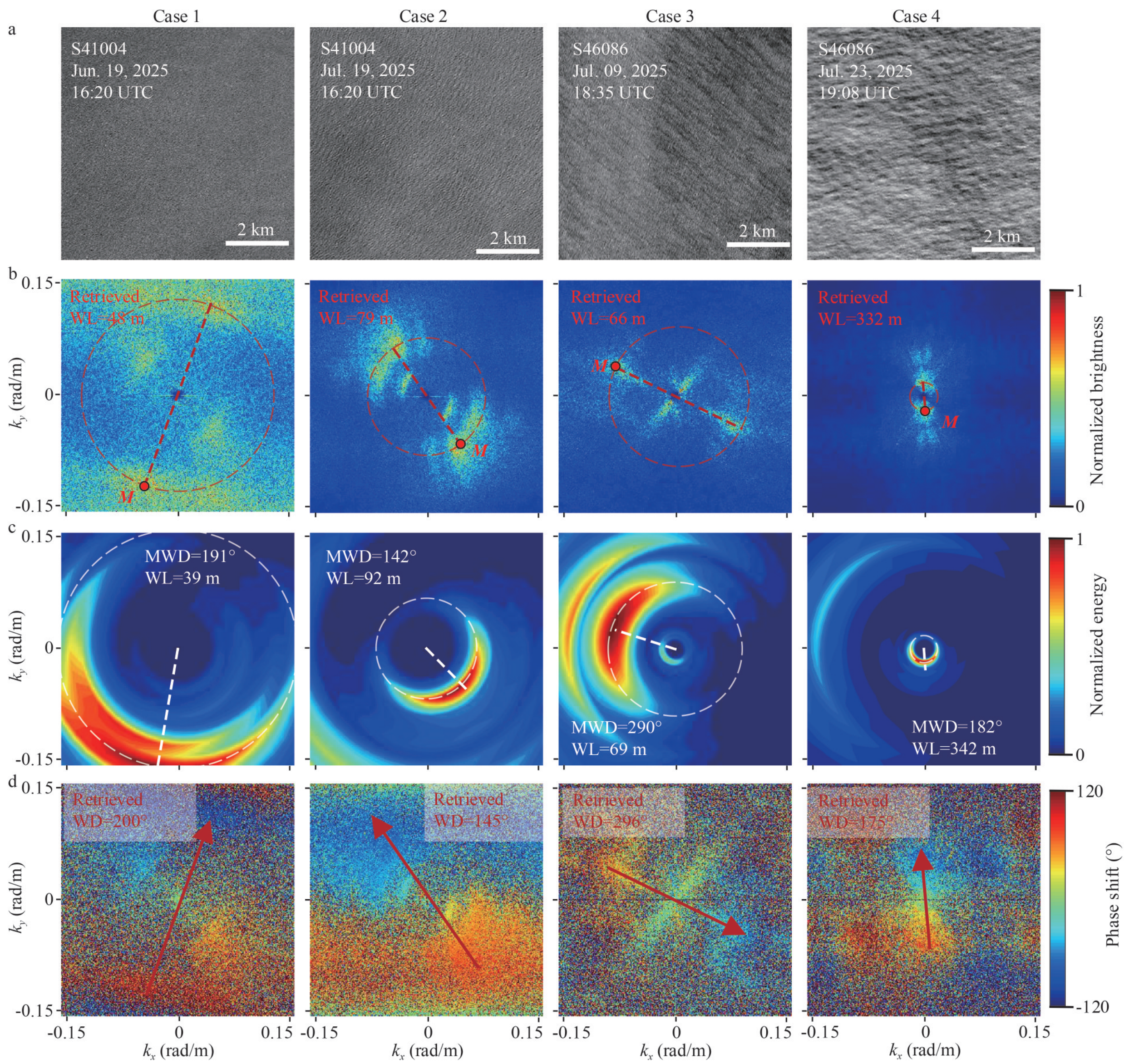

Fig.6 CZI-retrieved wave parameters and verified by in-situ buoy measurements

a. CZI B7 images; b. FFT spectra; c. in-situ buoy wave spectra; d. P (B2, B7) for 4 matched cases. WL: wavelength; FFT: Fast Fourier Transform; WD: wave direction; MWD: mean wave direction.

period swell of case 4, the CZI-derived parameters show good agreement with buoy observations. The comparison of WD, WL, and dominant period (PD) between the CZI retrievals and in-situ measurements is summarized in Table 2.

Figure 7 presents the validations for the 69 CZI-ERA5 matchups. Since ERA5 does not provide WL products, the comparison focuses on MWD and MWP. The retrieved WD agrees with ERA5 MWD with RMSE=20.50° and Bias=0.24°, and the retrieved wave period agrees with ERA5 MWP with RMSE=1.68 s and Bias=0.10 s. Note that the CZI retrieval window is 8 km×8 km, whereas ERA5 wave products have a spatial resolution of 0.5°. Therefore, there is the spatial-temporal mismatch in the comparison. The cases with mismatch were excluded from the linear statistics, and the associated uncertainty analysis is provided in Section 4.1.

Overall, these results support the feasibility of the proposed method and demonstrate the capability of CZI multispectral observations for monitoring ocean surface wave dynamics.

3.3 Cross-channel characteristics of different focal plane

The time lag of CZI has been clarified in Section 3.1. Beyond this temporal offset, the CZI dual-focal plane design means that incident light in different channels follows distinct optical paths before being synthesized on the CCD sensor. The fused image from the two focal planes introduces a small but systematic along-track (flight direction) misregistration of approximately 1–3 pixels. As a consequence, the phase shift between cross-focal plane channels can cause severe spectral distortion, thereby compromising the reliability of ambiguity removal in wave detection. Figure 8 illustrates the inter-focal plane phase shift and the corresponding coherence-phase shift spectra (CPS) for four cases. The CPS is computed as:

$$\mathrm{CPS}=\begin{cases}0, & C<0.1\\ P, & C\geq 0.1\end{cases}. \tag{10}$$

The rainbow-colored images in Fig.8 show the relative phase shifts between selected bands, whereas the black background images depict the CPS. Since band B2 is the earliest acquired channel among all CZI bands, it was used as the reference with bands B3, B5, and B7, all of which are located on the reflection focal plane. The white dashed circles in the CPS mark the dominant wave energy clusters. These clusters exhibit clear phase shifts

Table 2 Comparison of CZI-retrieved with in-situ buoy wave parameters

Case ID	Buoy ID	Buoy MWD (°)	Retrieved WD (°)	Buoy DPD (s)	Retrieved PD (s)	Buoy WL (m)	Retrieved WL (m)
1	41004	191	200	5	4.7	39	48
2	41004	142	145	7.7	7.1	92	79
3	46086	290	296	6.7	7.4	69	66
4	46086	182	175	14.8	11.8	342	332

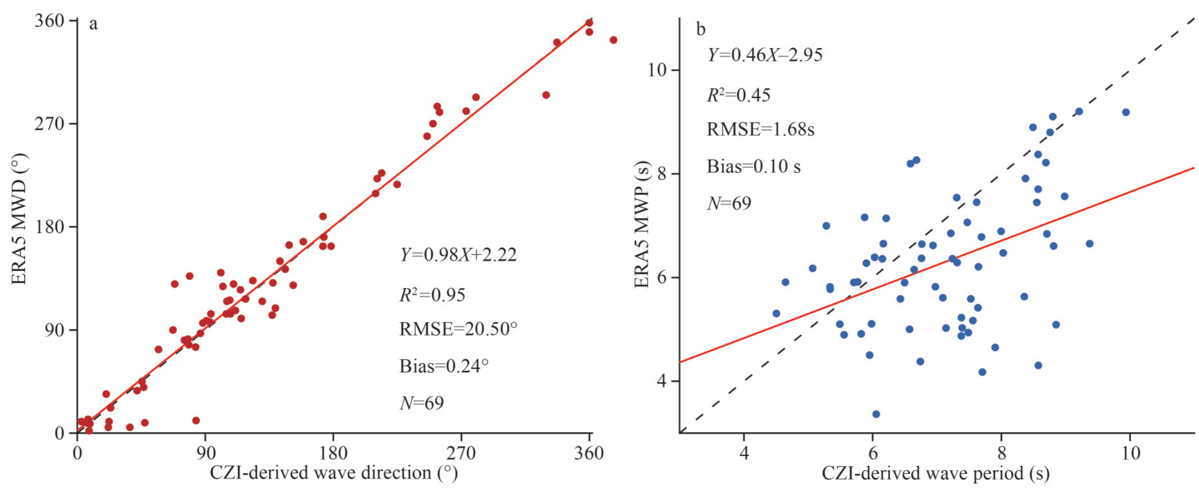

Fig.7 CZI-retrieved wave parameters and verified by ERA5 wave products

a. the statistical relationship between 69 CZI-derived wave direction and ERA5 MWD; b. the statistical relationship between CZI-derived wave period and ERA5 MWP. MWD: mean wave direction; MWP: mean wave period.

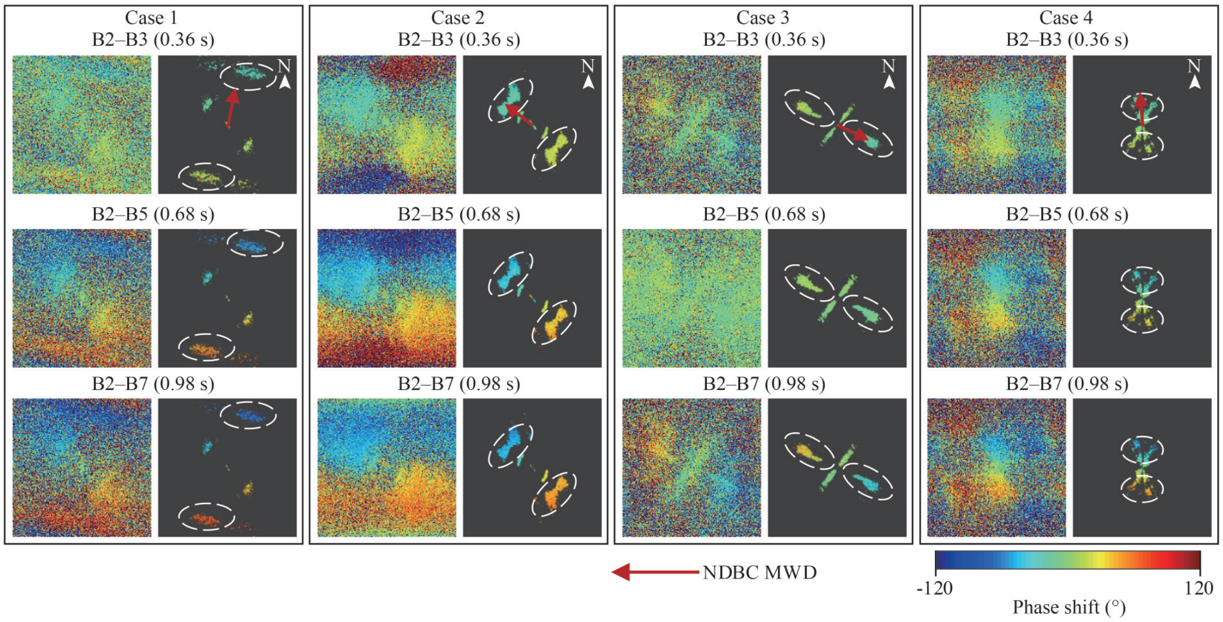

Fig.8 Inter-focal plane phase shift for 4 cases

The rainbow-colored images show the phase shift of the selected channel, and the black background images are the corresponding CPS. The white dashed circles represent wave energy clusters.

consistent, with larger inter-band time lags leading to more pronounced phase shifts. The wave energy clusters are uniformly distributed, and the direction from positive to negative aligns consistently with in-situ wave measurements.

In contrast, Fig.9 shows the phase shift between B2 (reflection focal plane) and bands B1, B4, B6, and B8 (transmission focal plane). The phase shift among these cross-focal plane pairs display marked energy distortions, as highlighted by the white dashed circles. The distorted spectral energy consistently aligns from the north-northeast toward the south-southwest direction (i.e., the flight direction of HY-1E). Notably, the smaller the inter-band time lags, the more pronounced the distortion. These distortions introduce significant phase anomalies in the CPS (yellow dashed circles). In case 1 and case 4, the direction from positive to negative of wave energy cluster is opposite to the buoy-measured WD, leading to incorrect ambiguity removal. Although such distortions do not produce incorrect propagation directions in case 2 and case 3, they cause strong irregular in the energy distribution.

These findings demonstrate that the specific channel configuration of the CZI sensor can induce substantial spectral anomalies in cross-focal-plane spectral analysis. Therefore, wave retrieval algorithms should employ the channel pairs within the same focal plane, such as B2, B3, B5, and B7 for the reflection or B1, B4, B6, and B8 for the transmission focal plane, to avoid such systematic phase anomalies.

3.4 Application in offshore case study

While the methodology and its characteristics have been demonstrated, the key is how the proposed workflow can be applied to large-scale imagery, particularly to exploit the advantages of high spatial resolution and nearshore monitoring capability. This section shows two full-scene CZI applications over coastal regions of China and the United States.

Figure 10a shows a full-scene CZI B7 image along the coast of the Shandong Peninsula, China, on 20 March 2025 at 02:54 UTC, while Fig.11a displays a scene off the coast of South Carolina, USA, on 19 July 2025 at 16:20 UTC. A sliding-window approach of 4 km×4 km (200×200 pixels) was applied to compute WD and WL using the proposed method. Blue circles indicate cloud areas, where wave retrieval was not feasible. The resulting wave products are shown in Figs.10b & 11b, both scenes exhibit wave systems propagating from the southeast toward the northwest, with WLs retrieved simultaneously in the same product. Gray areas represent regions where optical retrieval was disabled by cloud cover. To assess the retrieval

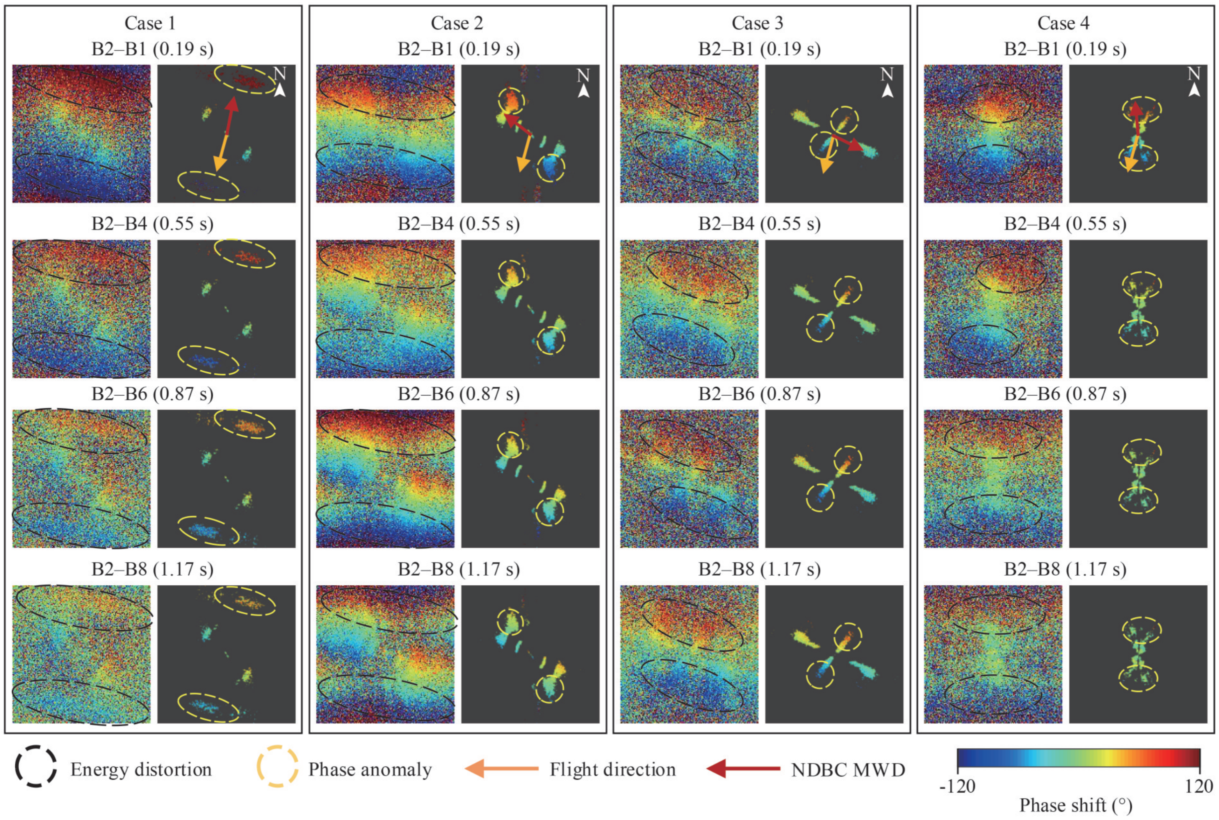

Fig.9 Cross-focal plane phase shift for 4 cases

The rainbow-colored images show the phase shift of the selected channel, and the black background images are the corresponding CPS. The black dashed circles represent energy distortion caused by different focal plane, and the yellow dashed circles represent distortion-induced phase anomalies.

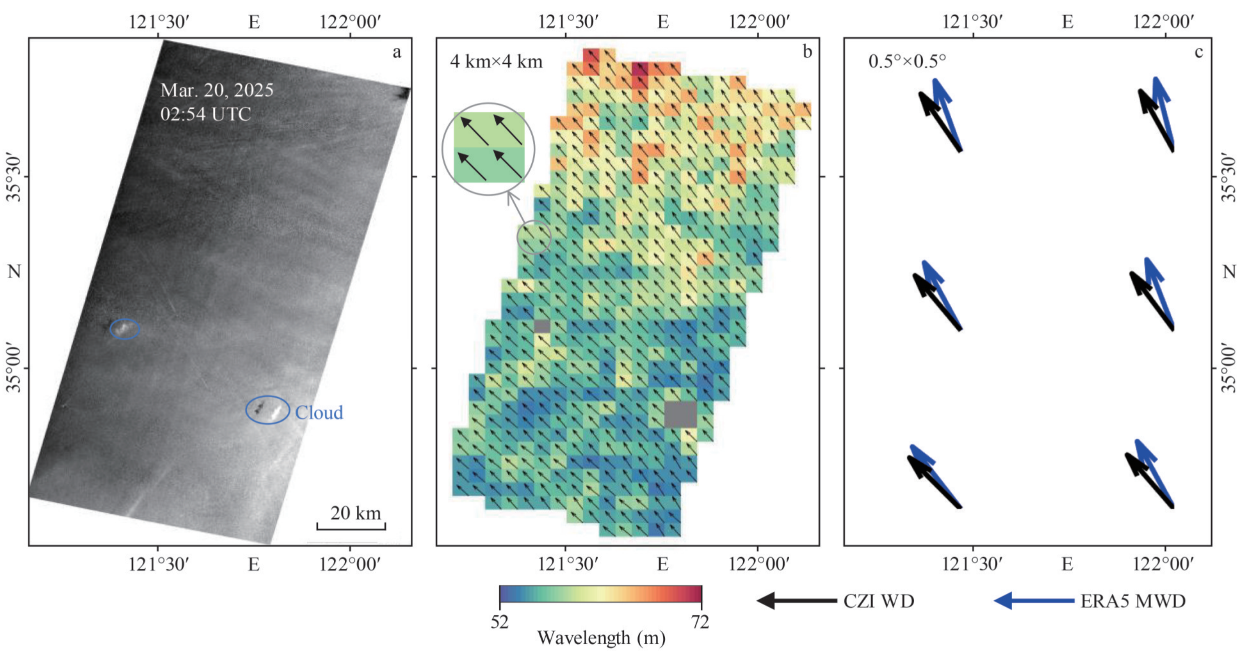

Fig.10 CZI-derived coastal wave product compared with ERA5 product

a. CZI B7 image in the offshore Shandong Province, China; b. CZI-derived wave direction and wavelength products (4-km spatial resolution); c. comparison of CZI wave direction (binned to 0.5°) with EAR5 wave product (0.5° spatial resolution). WD: wave direction; MWD: mean wave direction.

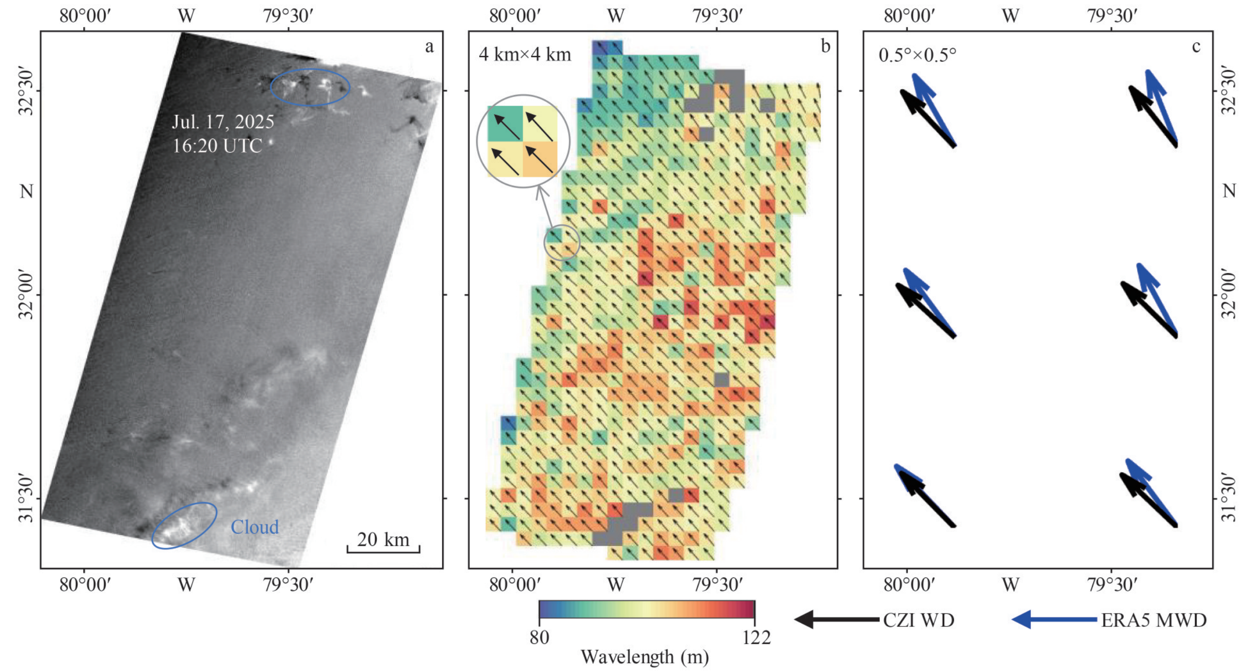

Fig.11 CZI-derived coastal wave product compared with ERA5 product

a. CZI B7 image in the offshore South Carolina, USA; b. CZI-derived wave direction and wavelength products (4-km spatial resolution); c. comparison of CZI wave direction (binned to 0.5°) with EAR5 wave product (0.5° spatial resolution). WD: wave direction; MWD: mean wave direction.

accuracy, the 4-km windows were spatially binned to 0.5° resolution and compared with the corresponding ERA5 wave products. Because ERA5 does not provide WL product, only WD was evaluated. As shown in Figs.10c & 11c, the CZI-derived WDs (black arrows) agree well with the hourly ERA5 WD products, with RMSE of 11.75° and 8.28°, respectively. These results confirm the superior performance and accuracy of the CZI sensor in producing large-scale wave products.

4 DISCUSSION

4.1 Uncertainty in comparison with ERA5 products

Since ERA5 reanalysis data are model-derived products rather than in-situ measurements, direct comparison between ERA5 wave products and CZI-derived wave parameters inherently involves uncertainties related to spatial representativeness and sea-state consistency.

Figure 12 illustrates four representative cases that highlight the limitations of validation against ERA5. In the matchups of this study, the maximum temporal interval between CZI observations and ERA5 product is 30 min, and the spatial separation is 0.25°, which means that the wave field in the 8-km×8-km CZI segment not always correspond to the ERA5 grid. For example, in the upper-left case, the wave system by ERA5 is mismatched in in the CZI imagery. The upper-right case illustrates a mixed sea state with multiple wave systems, where the CZI- retrieved wave system are differ from the ERA5 reported dominant system. The lower-left case illustrates impact under an unstable MABL, where the air-sea temperature difference is 1.6 °C and convective cell structures can be observed. Under such conditions, the rapid changes of air sea state result in the mismatch of ERA5 and CZI products. The lower-right case demonstrates that under weak sunglint conditions, reduced image signal-to-noise ratio can suppress wave texture and lead to wave retrieval failure.

Overall, although ERA5 provides a useful large-sample reference for statistical evaluation, these cases highlight that ERA5-CZI comparisons are subject to uncertainties arising from spatial-temporal mismatch, mixed sea states, MABL instability, and observation conditions, and such factors should be considered in regional ocean dynamic monitoring.

4.2 Advantage of whitecap detection

The advantage of high spatial resolution remote sensing for sea surface monitoring is its ability to capture detailed wave texture features. During wave

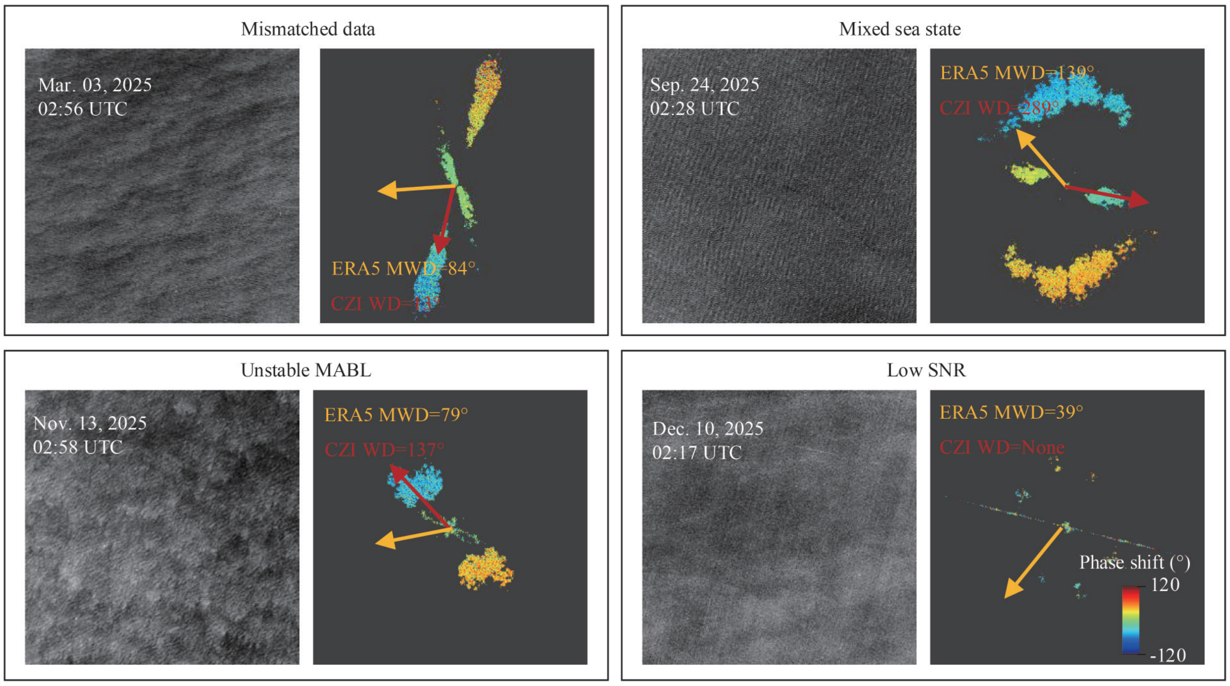

Fig.12 Uncertainties in comparing ERA5 wave product and CZI observation

The gray images are CZI B7 images, the black background images are the corresponding CPS. MWD: mean wave direction; WD: wave direction; MABL: marine atmospheric boundary layer; SNR: signal noise ratio.

breaking, entrained air forms strongly reflective bubbles known as whitecaps, which appear as bright features across all bands in high resolution optical imagery. Since wind is the primary driver of wave energy and governs dissipation, whitecap coverage is closely linked to surface wind conditions. Previous studies based on MSI and OLI imagery (Kubryakov et al., 2021; Zhao et al., 2022; Yin and Lu, 2025) have demonstrated a strong statistical relationship between whitecaps and sea surface wind speed. If whitecaps can be accurately extracted, statistical relationships between whitecap coverage and wind speed can be utilized to estimate surface winds.

The CZI sensor provides eight multispectral bands at 20-m resolution and a 5-m panchromatic band. Earlier research, based on extensive in-situ matched data, has established statistical relationships between wind speed and whitecap coverage W for Sentinel-2 MSI (10 m) and Landsat OLI (30 m). However, these relationships are dependent due to scale effects of remote sensing. CZI imagery also exhibits rich whitecap features as shown in the 20-m B7 band (Fig.13a) and the corresponding 5-m panchromatic band (Fig.13b). Using curvature filtering combined with OTSU threshold segmentation, the extracted whitecap distributions (Fig.13a3, a4, b3, b4) reveal that higher resolution imagery provides more accurate descriptions of whitecap distributions and fine-scale surface textures. Nevertheless, the overall whitecap coverage remains consistent across different spatial resolutions for the same region. This indicates that both the multispectral and panchromatic bands of CZI are capable of reliable whitecap detection.

Due to the limited dataset available in this study, it is unable to develop new empirical wind speed-whitecap coverage models for the CZI sensor. Future work, supported by larger match-up datasets, should aim to establish such models for both the 5-m and the 20-m multispectral bands. The comprehensive monitoring of sea surface wind and wave parameters using high resolution Chinese optical satellite data holds great promise for the future.

5 CONCLUSION

In this study, the specific imaging configuration of the HY-1E CZI sensor was systematically analyzed and the resulting inter-channel time lags were quantified. A specialized wave parameter retrieval workflow for the CZI instrument was developed. The approach was validated using matched in-situ and ERA5 matchup pairs. The CZI-derived WD and period agree well with ERA5

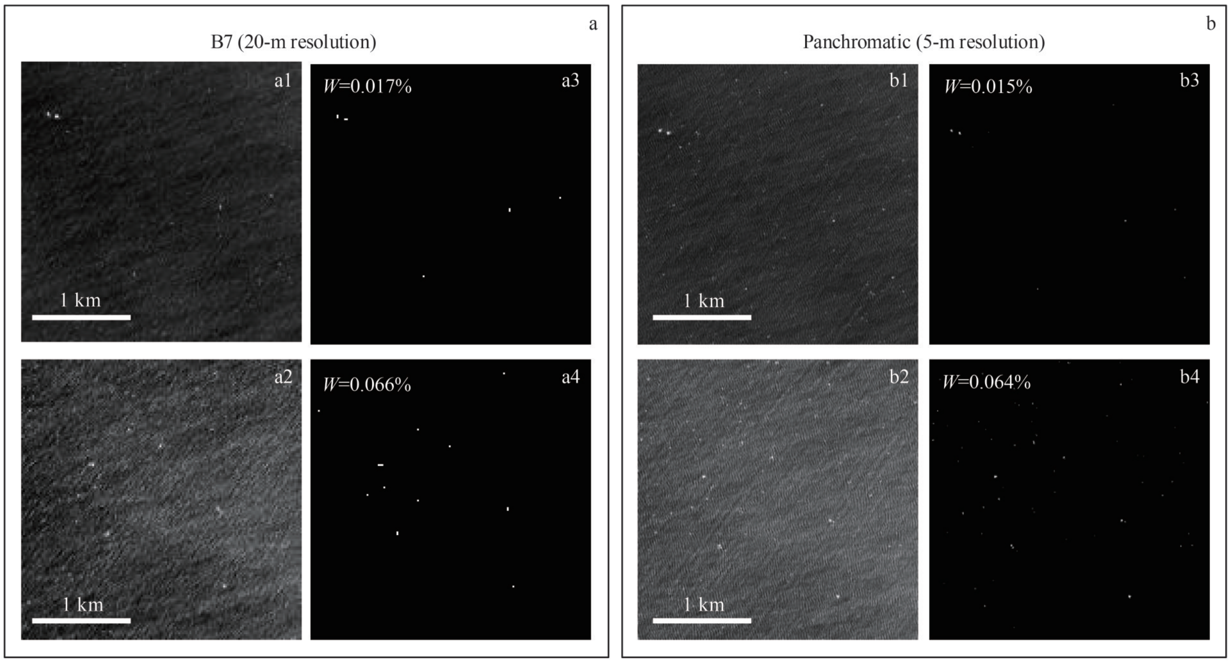

Fig.13 Whitecap feature in the CZI images

a. CZI B7 images and identified whitecaps; b. corresponding panchromatic images and identified whitecap. The gray images are CZI images, the black background images are the extracted whitecaps.

reanalysis, with an RMSE of 20.50° and 1.68 s, and a Bias of 0.24° and 0.10 s, respectively. Cross-focal plane spectral analysis confirmed that channel pairs among the same focal plane can effectively resolve the 180° directional ambiguity in wave propagation, whereas across-focal planes introduce spectral distortion and lead to incorrect estimation. The applicability of the method was further verified through large-scale coastal case studies, with retrieved WDs showing agreement with ERA5 reanalysis data (RMSE<12°). Additionally, the uncertainties in comparison with ERA5 products have been assessed, and the potential of multispectral and panchromatic bands for whitecap extraction was discussed, highlighting their combined monitoring of wind and wave fields. In conclusion, the HY-1E CZI sensor demonstrates strong capability for sea surface wave observation and provides a reliable data source for dynamical studies in coastal environments.

6 DATA AVAILABILITY STATEMENT

All data generated and/or analyzed during this study are available from the following sources: HY-1E CZI data (https://osdds.nsoas.org.cn/DataRetrieval); NDBC buoy data (https://www.ndbc.noaa.gov); ERA5 data (https://cds.climate.copernicus.eu/datasets/reanalysis-era5-single-levels?tab=download).

References

Bai R F, He X Q, Ye X M et al. 2025. Development of the operational atmospheric correction algorithm for the COCTS2 onboard the Chinese new-generation ocean color satellite. *Optics Express*, **33**(18): 38029-38053, https://doi.org/10.1364/OE.566718.

Bergsma E W J, Almar R, Maisongrande P. 2019. Radon-augmented Sentinel-2 satellite imagery to derive wave-patterns and regional bathymetry. *Remote Sensing*, **11**(16): 1918, https://doi.org/10.3390/rs11161918.

Cox C, Munk W. 1954. Measurement of the roughness of the sea surface from photographs of the sun’s glitter. *Journal of the Optical Society of America*, **44**(11): 838-850, https://doi.org/10.1364/JOSA.44.000838.

De Michele M, Leprince S, Thiébot J et al. 2012. Direct measurement of ocean waves velocity field from a single SPOT-5 dataset. *Remote Sensing of Environment*, **119**: 266-271, https://doi.org/10.1016/j.rse.2011.12.014.

De Michele M, Raucoules D, Arason Þ. 2016. Volcanic Plume Elevation Model and its velocity derived from Landsat 8. *Remote Sensing of Environment*, **176**: 219-224, https://doi.org/10.1016/j.rse.2016.01.024.

European Space Agency. 2015. Sentinel-2 User Handbook, https://sentinels.copernicus.eu/documents/247904/685211/Sentinel-2_User_Handbook.

Fan S R, Zhang B, Moiseev A et al. 2023. On the use of dual co-polarized radar data to derive a sea surface Doppler model—Part 2: simulation and validation. *IEEE Transactions on Geoscience and Remote Sensing*, **61**: 4202009, https://doi.org/10.1109/TGRS.2023.3246771.

Hao M Y, Hu Y Y, Shao W Z et al. 2025. Advance in sea surface wind and wave retrieval from synthetic aperture radar image: an overview. *Journal of Ocean University* *of China*, **24**(4): 821-839, https://doi.org/10.1007/s11802-025-6065-y.

Hasselmann K, Hasselmann S. 1991. On the nonlinear mapping of an ocean wave spectrum into a synthetic aperture radar image spectrum and its inversion. *Journal of Geophysical Research*: *Oceans*, **96**(C6): 10713-10729, https://doi.org/10.1029/91JC00302.

Hauser D, Tison C, Amiot T et al. 2017. SWIM: the first spaceborne wave scatterometer. *IEEE Transactions on Geoscience and Remote Sensing*, **55**(5): 3000-3014, https://doi.org/10.1109/TGRS.2017.2658672.

Hu C M, Li X F, Pichel W G et al. 2009. Detection of natural oil slicks in the NW Gulf of Mexico using MODIS imagery. *Geophysical Research Letters*, **36**(1): L01604, https://doi.org/10.1029/2008GL036119.

Jackson C R, Alpers W. 2010. The role of the critical angle in brightness reversals on sunglint images of the sea surface. *Journal of Geophysical Research*: *Oceans*, **115**(C9): C09019, https://doi.org/10.1029/2009JC006037.

Kubryakov A A, Kudryavtsev V N, Stanichny S V. 2021. Application of Landsat imagery for the investigation of wave breaking. *Remote Sensing of Environment*, **253**: 112144, https://doi.org/10.1016/j.rse.2020.112144.

Kudryavtsev V, Yurovskaya M, Chapron B et al. 2017a. Sun glitter imagery of ocean surface waves. Part 1: directional spectrum retrieval and validation. *Journal of Geophysical Research*: *Oceans*, **122**(2): 1369-1383, https://doi.org/10.1002/2016JC012425.

Kudryavtsev V, Yurovskaya M, Chapron B et al. 2017b. Sun glitter imagery of surface waves. Part 2: waves transformation on ocean currents. *Journal of Geophysical Research*: *Oceans*, **122**(2): 1384-1399, https://doi.org/10.1002/2016JC012426.

Liu Y X, Xu B H, Zhi W F et al. 2020. Space eye on flying aircraft: from Sentinel-2 MSI parallax to hybrid computing. *Remote Sensing of Environment*, **246**: 111867, https://doi.org/10.1016/j.rse.2020.111867.

Lygre A, Krogstad H E. 1986. Maximum entropy estimation of the directional distribution in ocean wave spectra. *Journal of Physical Oceanography*, **16**(12): 2052-2060, https://doi.org/10.1175/1520-0485(1986)016<2052:MEEOTD>2.0.CO;2.

Ma T, Xu Q, Yin X B et al. 2026. A physics-enhanced deep-learning model for estimating turbid shallow water depth from SAR images. *Journal of Oceanology and Limnology*, **44**(1): 36-49, https://doi.org/10.1007/s00343-025-5008-1.

Mouche A, Chapron B, Knaff J et al. 2019. Copolarized and cross-polarized SAR measurements for high-resolution description of major hurricane wind structures: application to Irma category 5 hurricane. *Journal of Geophysical Research*: *Oceans*, **124**(6): 3905-3922, https://doi.org/10.1029/2019JC015056.

Stopa J E, Wang C, Vandemark D et al. 2022. Automated global classification of surface layer stratification using high-resolution sea surface roughness measurements by satellite synthetic aperture radar. *Geophysical Research Letters*, **49**(12): e2022GL098686, https://doi.org/10.1029/2022GL098686.

Wang C, Tandeo P, Mouche A et al. 2019. Classification of the global Sentinel-1 SAR vignettes for ocean surface process studies. *Remote Sensing of Environment*, **234**: 111457, https://doi.org/10.1016/j.rse.2019.111457.

Wang L F, Lu Y C, Hu C M. 2025a. A practical angular spectrum method to estimate ocean surface wave directions and wavelengths using Sentinel-2 MSI imagery. *Remote Sensing of Environment*, **331**: 115044, https://doi.org/10.1016/j.rse.2025.115044.

Wang L F, Lu Y C, Wang M X et al. 2025b. Spatial resolution and channel time lag requirement of optical satellite sensors for ocean wave monitoring. *IEEE Geoscience and Remote Sensing Letters*, **22**: 1504405, https://doi.org/10.1109/LGRS.2025.3611634.

Wang Y H, Xu X G, Dong Z M. 2025c. An improved one-dimensional ocean wave description based on SWIM observations. *Atmospheric Measurement Techniques*, **18**(21): 6329-6344, https://doi.org/10.5194/amt-18-6329-2025.

Yin Z Y, Lu Y C. 2025. Optical quantification of wind-wave breaking and regional variations in different offshore seas using Landsat-8 OLI images. *Journal of Geophysical Research*: *Atmospheres*, **130**(1): e2024JD041764, https://doi.org/10.1029/2024JD041764.

Yin Z Y, Lu Y C, Liu Y R et al. 2024. Monitoring discharge from deep-sea mining ships via optical satellite observations. *Journal of Oceanology and Limnology*, **42**(6): 1853-1864, https://doi.org/10.1007/s00343-024-3264-0.

Yurovskaya M, Kudryavtsev V, Chapron B et al. 2019. Ocean surface current retrieval from space: the Sentinel-2 multispectral capabilities. *Remote Sensing of Environment*, **234**: 111468, https://doi.org/10.1016/j.rse.2019.111468.

Yurovskaya M, Rascle N, Kudryavtsev V et al. 2018. Wave spectrum retrieval from airborne sunglitter images. *Remote Sensing of Environment*, **217**: 61-71, https://doi.org/10.1016/j.rse.2018.07.026.

Zhang B, Li X F, Perrie W et al. 2015. Synergistic measurements of ocean winds and waves from SAR. *Journal of Geophysical Research*: *Oceans*, **120**(9): 6164-6184, https://doi.org/10.1002/2015JC011052.

Zhang K L, Wang L L, Yan C. 2025a. System design and develop of the new-generation ocean color observation satellite. *Spacecraft Recovery & Remote Sensing*, **46**(2): 27-39, https://doi.org/10.3969/j.issn.1009-8518.2025.02.003. (in Chinese with English abstract)

Zhang X H, Chu B, Zheng J et al. 2025b. Design and verification of the Coastal Zone Imager on the new generation ocean color satellite. *Spacecraft Recovery & Remote Sensing*, **46**(2): 40-48, https://doi.org/10.3969/j.issn.1009-8518.2025.02.004. (in Chinese with English abstract)

Zhao B, Lu Y C, Ding J et al. 2022. Discrimination of oceanic whitecaps derived by sea surface wind using Sentinel-2 MSI images. *Journal of Geophysical Research*: *Oceans*, **127**(11): e2021JC018208, https://doi.org/10.1029/2021JC018208.

Zheng J, Zhang X M, Liu H et al. 2025. Design of the line-of-sight direction of the wide-swath coastal zone imager. *Spacecraft Recovery & Remote Sensing*, **46**(2): 72-85, https://doi.org/10.3969/j.issn.1009-8518.2025.02.007. (in Chinese with English abstract)